Full length article

Optimizing deployment dynamics of composite tape-spring hinges

Hao Jin [a], Ning An [b,c,*], Qilong Jia [d], Ruiwen Guo [a], Xiaofei Ma [e], Jinxiong Zhou [a]

[a] *State Key Laboratory for Strength and Vibration of Mechanical Structures and School of Aerospace, Xi'an Jiaotong University, Xi'an, 710049, People's Republic of China*
[b] *School of Aeronautics and Astronautics, Sichuan University, Chengdu, 610065, People's Republic of China*
[c] *State Key Laboratory of Structural Analysis for Industrial Equipment, Dalian University of Technology, Dalian, 116024, People's Republic of China*
[d] *Shanghai Jeatron Technology Co., Ltd, Shanghai, 201800, People's Republic of China*
[e] *Xi'an Institute of Space Radio Technology, Xi'an, 710100, People's Republic of China*

ARTICLE INFO

ABSTRACT

The composite tape-spring hinge (CTSH) is a lightweight structural connector widely employed in space structures, including spacecraft and satellites, due to its high specific strength and stiffness. Introducing cutouts enables CTSH to possess folding and deployment capability, while optimizing the cutouts finely to optimize the performance of CTSH. However, the interaction between cutout size and the dynamic deployment of CTSH is a novel topic. To address this, a multi-objective optimization problem is formulated, aiming to minimize both the maximum overshoot angle and deployment time while considering mass constraints. An accelerated size optimization is achieved by integrating data-driven surrogate modeling and size optimization. The optimized CTSH design exhibits a significant improvement in performance, with a 26.3% reduction in the maximum overshoot angle and a 12.6% reduction in the deployment time compared to the initial design. The proposed optimization strategy is highly adaptable and can be applied to various optimization problems, offering valuable insights for future designing space deployable structures with desirable performance.

1. Introduction

The Composite Tape Spring Hinge (CTSH) is obtained by making cutouts on a complete thin-walled composite tube. In addition to the lightweight, high specific stiffness, and high specific strength characteristics inherent in composite materials, the introduction of cutouts fully exploits the material's flexible properties, enabling the CTSH to be elastically folded into a small volume before and during launch and then unfold by releasing stored strain energy for use once in orbit. The advantages offered by CTSH position it as a potential replacement for traditional mechanical hinges in connection applications, and its ingenious concept has also inspired the design of novel deployable structures, such as deployable truss structures [1–4] and umbrella-type reflectors [5]. A milestone design involves connecting multiple CTSHs in series to form a boom. The boom undergoes multiple folding for storage prior to launch [6,7], and upon reaching the designated position, it is released from constraints and self-deploys through the release of stored strain energy. European Space Agency (ESA) successfully deployed antennas using this expandable boom in its Marsis mission (2003) and Juice mission (2023) [8], demonstrating the substantial potential of CTSH in space missions. Consequently, during the past decades, there has been a growing interest in both industry

and academia in analyzing and optimizing CTSHs. Numerous studies have been conducted to gain insights into the deployment dynamics of CTSHs, and optimization has emerged as a promising area for further investigation.

Understanding the dynamic deployment behavior of an individual CTSH is of great help through the experimental deployment test of a simplified boom model composed of aluminum tubes connected by CTSHs [9]. The experimental results of this model describe the general characteristics of CTSH's dynamic deployment: when a folded boom is released from constraints at a certain angle, the boom rapidly reaches its fully deployed straight configuration and attempts to lock. If the kinetic energy of the boom is too high, the CTSH bends to the other side (overshoot), followed by oscillation until the amplitude decays to zero. Excessive overshoot angles sharply increase the risk of structural damage. Alternative deployment schemes, such as introducing dampers or temperature-dependent viscoelastic effects, can control the overshoot angle but also slow down the deployment speed [10]. This means that achieving a balance between excessive and insufficient kinetic energy is challenging [11], especially for dynamic booms with multiple hinges [12]. These challenges are common for other boom designs, such as composite thin-walled lenticular tubes, which can be rolled up and

---

flattened to coil the boom but exhibit chaotic behavior when deployed without any control [13,14]. In conclusion, ensuring the deployment capability of CTSHs (without compromising deployment speed) while suppressing deployment shocks (minimizing overshoot angles as much as possible) is a key task and one of the main challenges in CTSH design.

The combination of multi-objective optimization and CTSH cutout design offers potential solutions to address this issue. Mallikarachchi and Pellegrino [15] conducted sensitivity analysis to investigate the influence of geometric parameters such as slot length, width, and end radius on the quasi-static folding and unfolding performance of composite tube hinges. Ye et al. [16] proposed an optimization design method for pure bending self-locking tape springs by combining response surface methodology (RSM) with large-scale generalized reduced gradient (LSGRG) optimization algorithm and reported a 19.5% increase in steady-state torque while satisfying maximum stress constraints. Yang et al. [17] conducted multi-objective optimization design research on a dual-layer metal tape spring hinge using an improved non-dominated sorting genetic algorithm II (NSGA-II), with steady-state moment and peak moment as two optimization objectives for quasi-static unfolding of the hinge. Liu et al. [18] formulated the optimization problem of CTSH to obtain three conflicting objectives: minimizing peak folding moment, maximizing peak bending moment, and minimizing mass. Ferraro et al. developed two methods (a level set function approach for topology optimization and a spline representation for shape optimization) to design irregular cutout shapes that allow damage-free folding and maximize CTSH stiffness [19]. Jin et al. proposed an accelerated optimization strategy for cutout shape to simultaneously enhance the maximum stored strain energy and quasi-static unfolding moment of CTSH [20]. P. Fernandes et al. optimized the CTSH cutout shape using genetic algorithms to maximize the first natural frequency while avoiding folding damage [21]. In summary: (1) various performance metrics related to CTSH folding and unfolding exhibit high sensitivity to the dimensions or shapes of the cutout; (2) the combination of multi-objective optimization algorithms and numerical simulation in cutout optimization significantly improves CTSH folding and unfolding performance gains. However, all the aforementioned optimization work only considers CTSH under quasi-static conditions. Hence, optimizing cutout dimensions to concurrently minimize the deployment time and overshoot angle during the dynamic unfolding process of CTSH constitutes a noteworthy research.

Over the past few decades, numerous computational models have been developed to simulate the folding and unfolding processes of CTSH in order to replace costly experiments. These models utilize commercial finite element software packages such as Nastran, Ansys, LS-Dyna, and Abaqus [22–26]. Among them, Abaqus has powerful capabilities to analyze the highly nonlinear behavior of CTSH, including significant geometric changes associated with buckling and dynamic collapse. Mallikarachchi and Pellegrino [26,27] first compared the results of Abaqus/Explicit dynamic deployment simulations with experimental measurements of tape spring hinges made of carbon fiber-reinforced plastic composites, demonstrating the reliability of this numerical model. However, high-fidelity numerical simulations of CTSH deployment dynamics are not only highly nonlinear but also challenging to converge. Expensive Dynamic/Explicit solvers are required to ensure convergence. Additionally, the solution process needs to maintain synchronization between computational time steps and physical time, which means the use of any acceleration techniques to improve solution efficiency is forfeited. These circumstances have a catastrophic impact on the optimization design process involving a large number of objective function evaluations and variable sensitivity analyses. Therefore, surrogate or proxy models (RSM, Kriging, Neural Networks, Radial Basis Functions (RBF), Support Vector Networks (SVN) or Gaussian Process Regression (GPR), Moving Least Squares Method (MLSM), etc.) have been widely applied in structural design [28–32]. These approximation models express the relationship between the objective functions (outputs) and design variables (inputs)

through simple explicit functions or black-box functions, significantly reducing computational costs and exploring a wider design space. This has become a blessing for structural optimization problems involving hundreds or thousands of structural response calculations.

This paper seeks to enhance the dynamic unfolding performance of CTSH by combining the accelerated surrogate models and the optimization of cutout dimensions. Initially, we develop a platform to approximate the dynamic unfolding experiments of CTSH under zero-gravity conditions. Subsequently, we refine the high-fidelity finite element model based on the experiment results. We quantify the impact of cutout dimensions on the dynamic unfolding performance. Subsequently, we formulate a multi-objective size optimization problem for CTSH, aiming to minimize both the unfolding time and the maximum overshoot angle during the dynamic unfolding process, without altering the weight.

The structure of this paper is as follows: In Section 2, the dynamic unfolding experimental study of CTSH, the high-fidelity finite element modeling, and its unfolding mechanism are described. Additionally, the impact of varying cutout dimensions on CTSH behavior is quantified, highlighting the importance of size optimization. In Section 3, the rigorous mathematical formulation of the multi-objective optimization problem is presented, along with a detailed explanation of the implementation of surrogate modeling and the optimization problem. The results of the optimization are discussed in Section 4. Finally, some concluding remarks and future prospects are provided in Section 5.

2. Deployment dynamic mechanical behavior of CTSH

2.1. Experimental investigation

To enhance understanding of the CTSH's dynamic deployment behavior during service, a deployable boom structure was constructed by integrating the CTSH with an aluminum tube (see Fig. 1(a)). A steel mandrel with an outer diameter of 43 mm was coated with a mold release agent, and SKYFLEX K51 series USN100B prepreg tape was laid up in a $[\pm45]_2$ sequence. The prepreg tape had a thickness of 0.16 mm and contained 100 g of Torayca T700s carbon fibers per square meter. The mechanical properties of the prepreg tape are detailed in Table 1. The wrapped mandrel was further wrapped with BOPP films at a tension of 3 kg to secure the four layers of unidirectional tape. The curing process was accomplished through heating at 80 °C for 45 min, followed by 125 °C for 100 min. After cooling, the mandrel was removed, and six circular tubes with a length of 440 mm, inner diameter of 43 mm, and an average wall thickness of 0.4148 mm were obtained through cutting. Two parallel cuts were made on each CTSH, following three design schemes (A, B, and C) with the same mass, using a laser cutting machine with a manufacturing tolerance of ±0.05 mm (see Fig. 1(b)). Detailed dimensions can be found in Table 2, with each pair of hinges sharing the same design scheme. The CTSHs were connected to an aluminum tube with a thickness of 1 mm, an outer diameter of 43 mm, and a length of 820 mm. The aluminum tube is made of 6061 aluminum alloy [33], with a weight of 304.09 g, a Young's modulus of 68 MPa, and a Poisson's ratio of 0.33. The connection was achieved by inserting the aluminum tube into the CTSH with a 20 mm overlap and then covering and securing it with a hose clamp. The overall length of the structure was 1240 mm.

The experimental setup for the dynamic deployment test of the CTSH is shown in Fig. 2. The deployable boom was placed on a horizontal working table, and a 3 mm-thick hollow aluminum counterweight tube was attached to the rear end of the CTSH, offset by 20 mm. The aluminum tube was clamped and fixed with a bench clamp. The remaining parameters of the aluminum tube were the same as the previously mentioned one. A vertical rope with a diameter of 0.5 mm and a length of 10,000 mm was connected at the center of gravity of the 1 mm-thick aluminum tube and fixed to a framework directly above the center of gravity. This constraint permitted horizontal movement
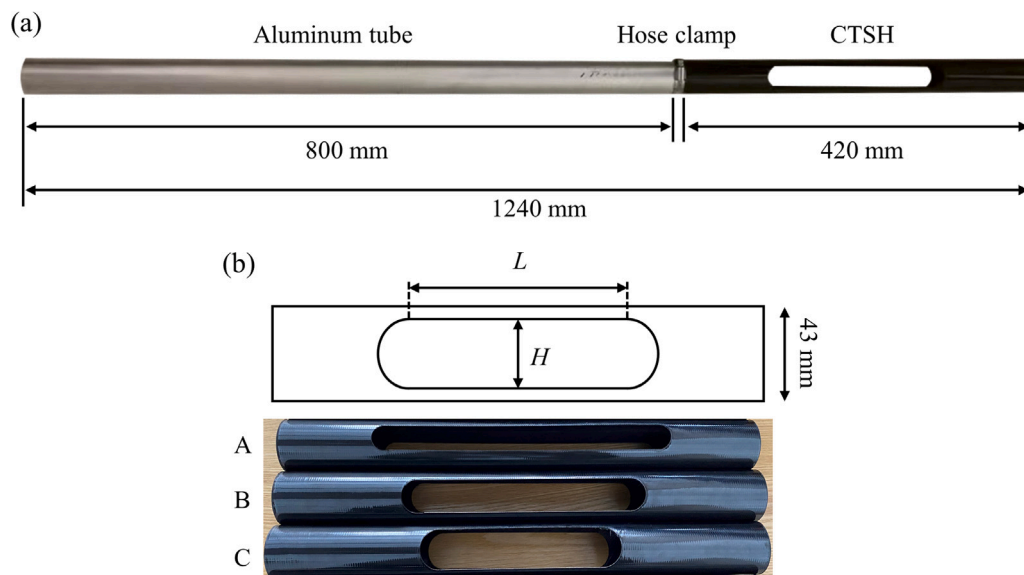
Fig. 1. Schematic diagram of a boom with a single CTSH at the root. (a) Fully deployed state of the CTSH connected to an aluminum tube (stress-free state). The CTSH has a length of 440 mm, the aluminum tube has a length of 820 mm, and the overlap measures 20 mm, resulting in a total length of 1240 mm. (b) Three CTSHs with approximately equal mass (≈ 29.94 g) are shown. The hinge is created by cutting two parallel slots on a carbon fiber-reinforced polymer composite tube. The tube has a diameter of 43 mm, an average wall thickness of 0.4148 mm, and a stacking sequence of $[\pm45]_2$. The geometric shape of the slots is characterized by their length (L) and width (H).
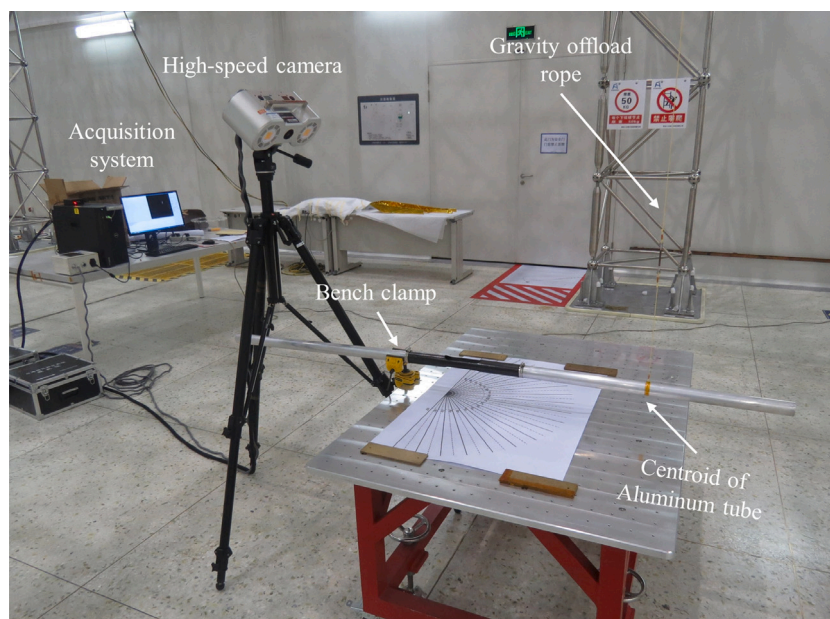

Fig. 2. Dynamic deployment experimental setup of CTSH with zero-gravity unloading condition.

of the boom. A white paper with black angular scale lines was placed directly below the boom to measure the deployment angle of the CTSH. A high-speed camera was fixed at the rear of the CTSH to capture the folding region, and the capture rate was set at 500 frames per second. The high-speed camera was connected to the MPS real-time industrial photogrammetry system. For each design scheme, the two CTSHs were folded at 45 degrees and then released once, while the high-speed camera recorded the deployment process. Subsequently, the identical test procedures were repeated with the opposite folding direction. A total of 12 tests were conducted. It is necessary to note that the cut-out size has a prominent effect on the folding deformation modes of CTSHs. Specifically, the CTSH with a longer and narrower slot tends to fold into a single central configuration, whereas the CTSH with a shorter and wider slot exhibits two equally likely potential folding configurations [27,34]. As shown in Fig. 3, Designs A and B

consistently fold into a single certain configuration, precisely folding at the center, while Design C exhibits two potential folding configurations, each occurring with equal probability in experiments, as demonstrated in *Case 1* and *Case 2*.

We developed a MATLAB program specifically designed to leverage the hough function for identifying the geometric shape outlines in each snapshot taken during the experiment. The hough transform is a technique in image processing that operates by mapping the image space into a parameter space. Within this parameter domain, geometric forms can be discerned through the recognition of distinct patterns [35,36]. The program detects the straight edges of the aluminum tube in each snapshot based on the capture sequence (with a time interval of 0.002s) and computes the angular deviation of the edges from their initial positions. It is important to note that the deployment angle is defined as 0 degrees when fully deployed and as a positive value when folded. This
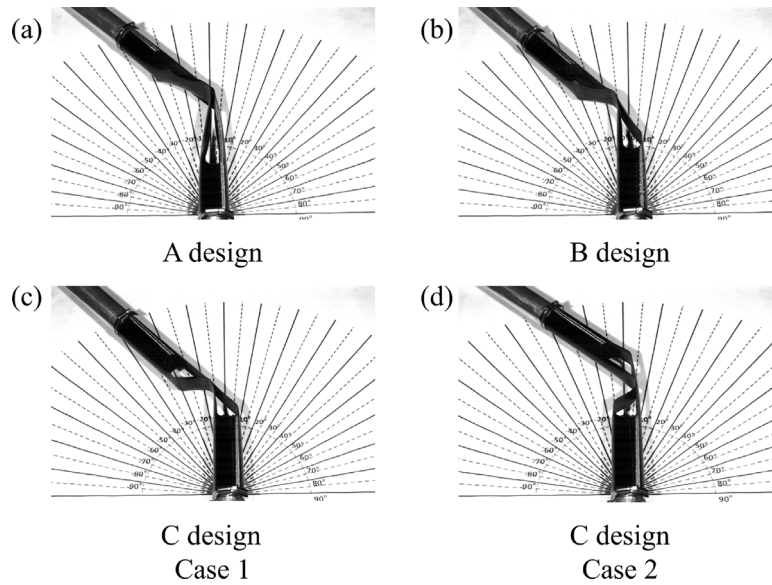
Fig. 3. Folding configurations of CTSHs with different cut-out sizes. (a) Design A and (b) Design B consistently fold into a unique configuration, whereas Design C exhibits two potential folding configurations, referred to as (c) *Case 1* and (d) *Case2*, respectively.

Table 1
Engineering constants of the prepreg tape (USN100B) [37].

E_{11} [GPa]	E_{22}, E_{33} [GPa]	G_{12}, G_{13} [GPa]	G_{23} [GPa]	v_{12}, v_{13}	v_{23}	t [mm]	ρ[g/cm^3]
88.931	7.601	5.407	2.631	0.335	0.492	0.1037	1.7326

enables the depiction of the deployment angle's temporal evolution, as exemplified in Figs. 4(a) and 4(b) with design scheme B. The results indicate that the deployment of the boom can be divided into three stages:

(1) The primary deployment stage encompasses the extension of the boom from the folded position at 45 degrees (represented by point 1 on the curve) to the initial fully deployed state (represented by point 2 on the curve). The deployment time, denoted as t_d^f, correlates with the deployment speed of the CTSH, with a smaller t_d^f indicating a more forceful deployment.

(2) Overshooting occurs when the boom fails to secure in the fully deployed state, resulting in buckling of the tape springs and causing the boom to fold in the opposite direction. This phenomenon, quantified by the maximum overshoot angle $\theta_d^{\max}$ (represented by point 3 on the curve), implies an increased risk of boom damage with larger $\theta_d^{\max}$ values.

(3) The vibration stage denotes the period during which the CTSH, after returning to the fully deployed state (point 4 on the curve), experiences minor oscillations around the equilibrium position until the amplitude completely diminishes.

The deployment angle versus time curves for multiple CTSH designs are compared in Fig. 4(c). It is clear that the dimensions L and H of the cuts have a significant impact on t_d^f and $\theta_d^{\max}$. Note that the dynamic deployment response of Design C differs from each other when the deployment starts from the folding configurations *Case 1* and *Case 2*, therefore two curves are presented for Design C. To further quantify the impact of the cut dimensions, a high-fidelity numerical analysis model was developed to simulate the experiments.

2.2. Numerical simulation analysis

The Abaqus/Explicit finite element package [38] is employed in this paper for all numerical calculations. ABAQUS/Explicit solver is employed to simulate the highly nonlinear behavior of CTSH folding and deployment, offering significant advantages in effectively handling convergence issues arising from complex contact and stiffness matrices.

Table 2
The cutouts size and mass of each design scheme of CTSH.

Scheme	L [mm]	H [mm]	M [g]
A	252	20	29.94
B	192	25	29.71
C	146	30	29.83

Fig. 5 depicts the comprehensive finite element model of the stress-free boom. The gray region represents the aluminum tube, discretized as a rigid body through R3D4 rigid elements. The mass of the entire region is coupled to reference point A positioned at the aluminum tube's centroid. The red region signifies the connecting tapes between the CTSH and the aluminum tube, segmented by S4R elements. The degrees of freedom of element nodes at the two connecting tapes are kinematically coupled to reference points B and C, respectively. Each reference point is assigned a mass of 20.94 g to simulate the weight of the tape region with clamps. The green region represents the CTSH, which is also modeled using S4R elements. The accuracy of the mesh was ascertained through a mesh refinement study, resulting in a meshing seed size of 2.8 mm and a total of 20,153 elements. The simulation analysis of the boom consists of two parts: a quasi-static folding at 45 degrees and a dynamic deployment. These are achieved through two analysis steps, each having specific boundary conditions and solver settings. In the first analysis step, the cross-sections coupled with C are fully constrained, including the translational degrees of freedom in the y - direction and the rotational degrees of freedom around the x and z axes of the cross-sections coupled with A and. Furthermore, point B is rotated by 45 degrees around the y - axis. In the second analysis step, starting from the 45-degree folded state, the rotational degree of freedom around the y - axis at point B is released, while the remaining boundary conditions remain unchanged. The solution time for both analysis steps is set to 2 s. In the folding analysis step, the focus is solely on achieving the correct folding state of the hinges, disregarding the physical significance of the solution time. To enhance analysis efficiency, the semi-automatic mass scaling technique
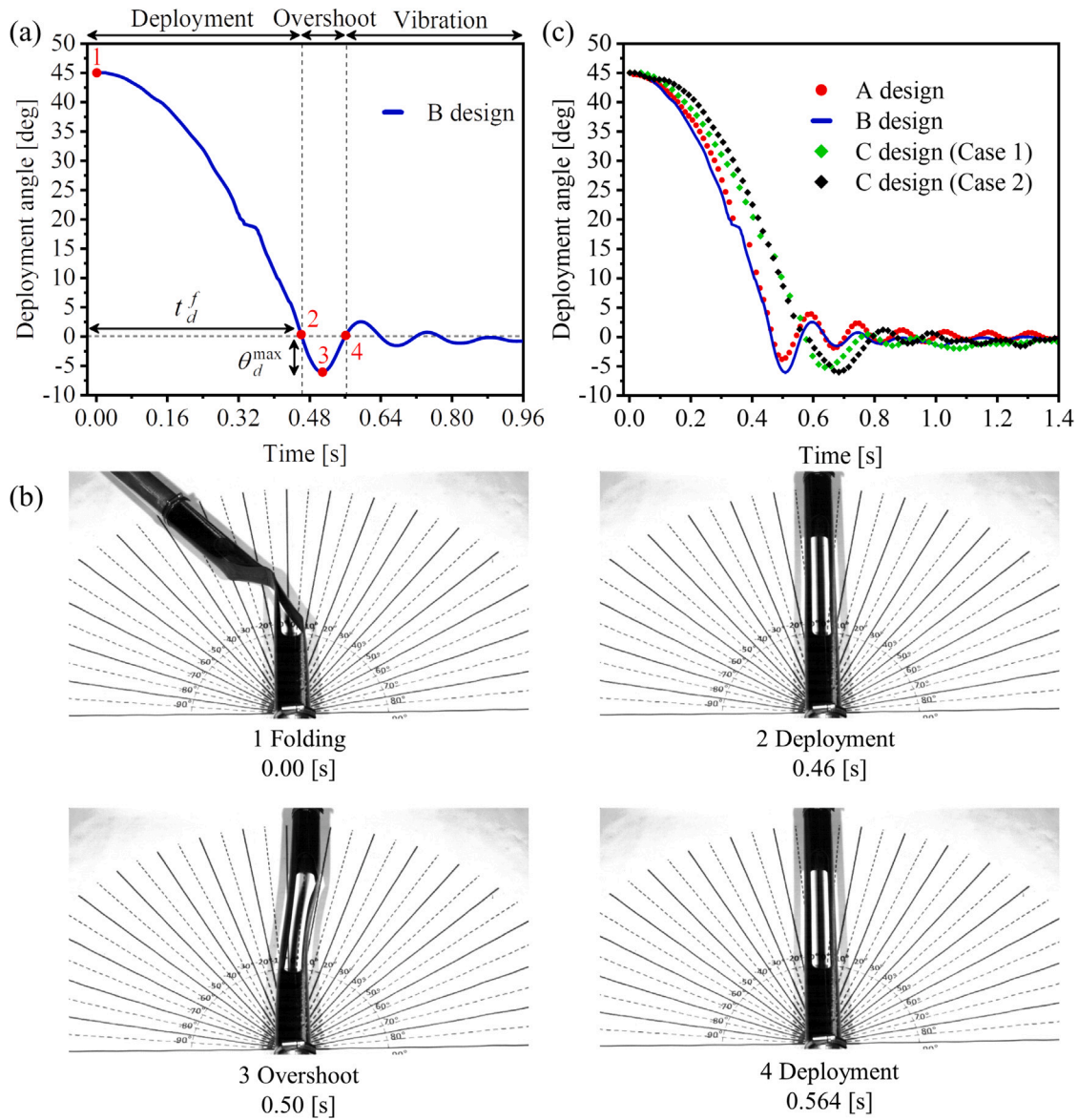
Fig. 4. Mechanical response of CTSH during dynamic unfolding (a) Variation of dynamic unfolding angle with time: (1) Main unfolding stage from point 1 to 2, with unfolding time t_d^f; (2) Overshoot stage from point 2 to 4, with maximum overshoot angle θ_d^{max} at point 3; (3) Vibration stage after point 4; (b) Key moments captured in the CTSH experiment (red dots labeled 1–4 in (a)); (c) Comparison of dynamic unfolding angles over time for CTSH with approximately equal mass (≈ 29.94 g) but different notch sizes by experiment.
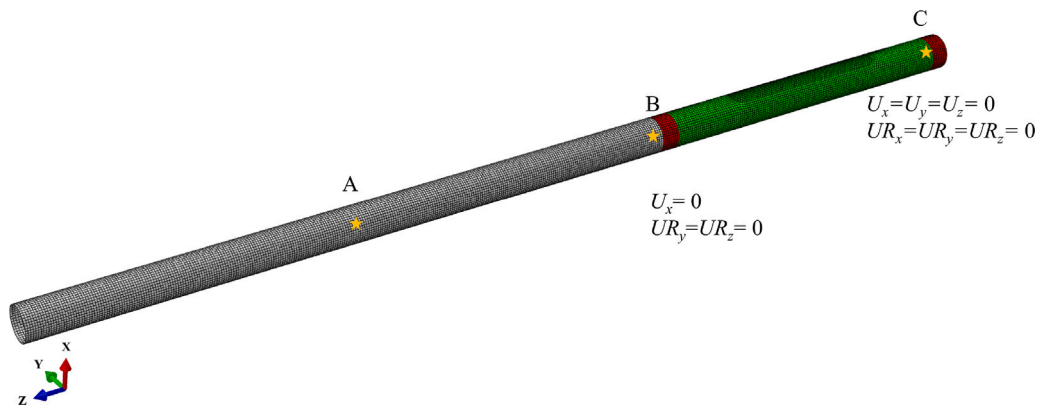

Fig. 5. Finite element model of the boom with mesh and boundary conditions. The gray region represents the aluminum tube, while the green region represents the CTSH. The nodes on the cross-section (highlighted in red) are kinematically coupled to reference points B and C, assuming rigid cross-sections at both ends of the CTSH. Reference point C is fully constrained, while reference point B is allowed movement in the y-z plane and is assigned a rotational angle around the x-axis (released during unfolding). The aluminum tube is treated as a rigid body, and point A represents the mass centroid. (For interpretation of the references to color in this figure legend, the reader is referred to the web version of this article.)
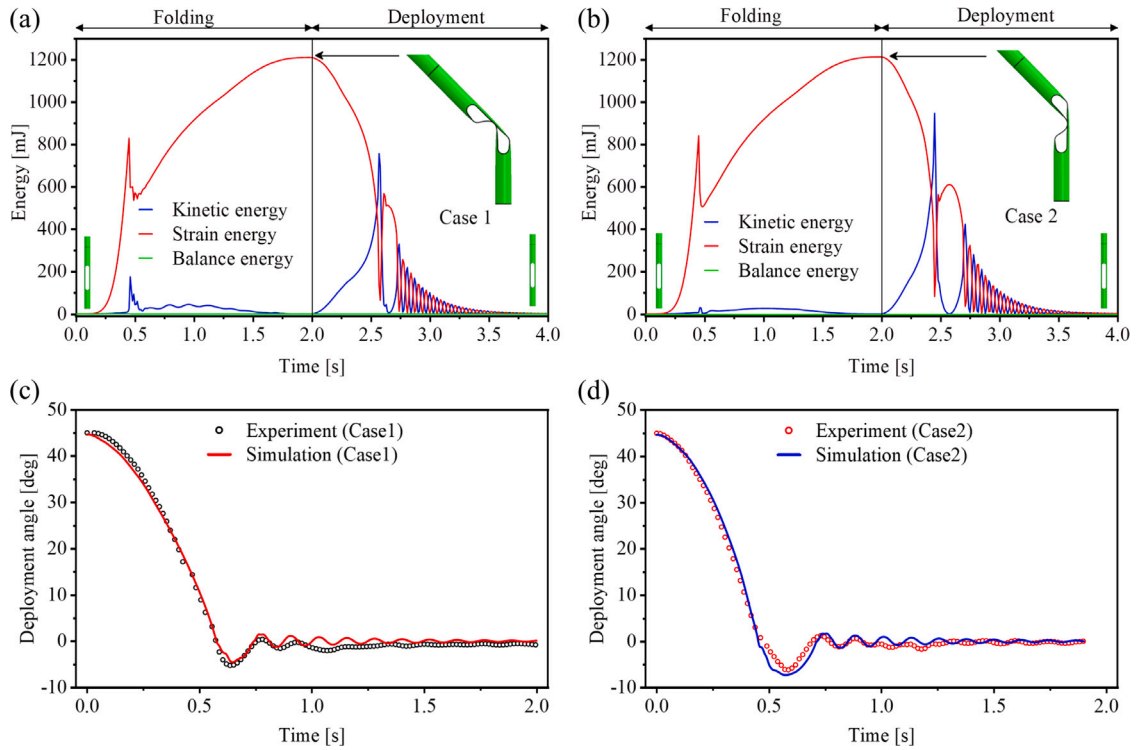
Fig. 6. Comparison of the deployment angle-time response between experiment and simulation. (a) and (b) respectively illustrate the energy variation over time during the quasi-static folding-dynamic unfolding simulation for cases 1 and 2 of the C-scheme CTSH. (c) and (d) provide a comparison of the experimental and simulation results for the dynamic response of the CTSH in the two different folding states.
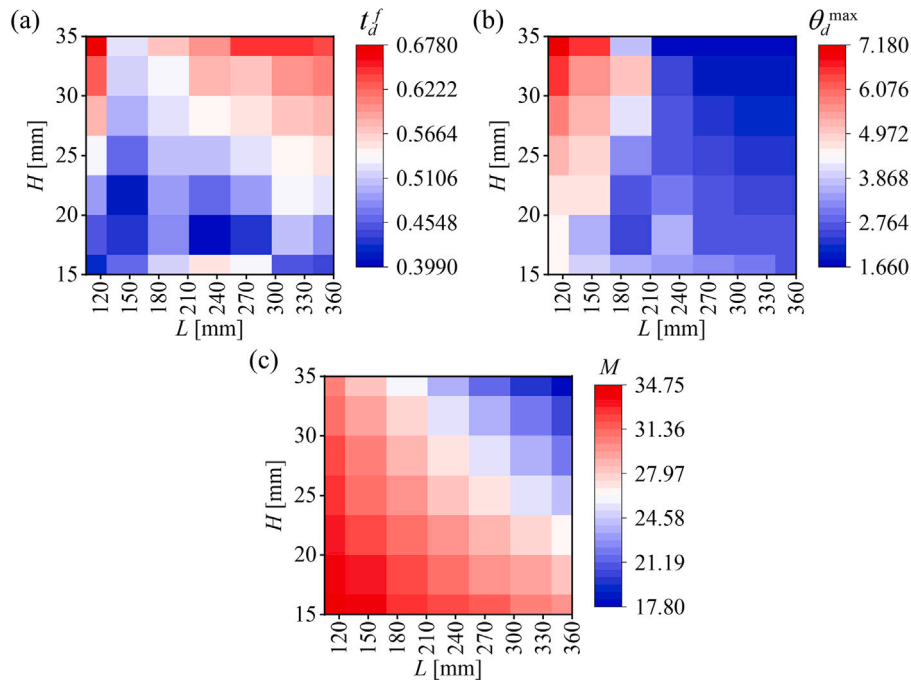

Fig. 7. Design space for the dynamic unfolding performance of CTSH in terms of cutout dimensions ($L \in [105, 360]$, $H \in [15, 35]$). Heatmap (a),(b) and (c) respectively displaying the distribution of t_d^f, θ_d^{max} and M as a function of L and H within the design space.

is utilized along with a smooth step (a fifth-order polynomial function of time) displacement loading profile to regulate the loading process. Furthermore, the Explicit solver employs a stable time increment of 1×10^{-6}. Upon entering the second analysis step, the mass scaling switch is deactivated, and the deployment angle is recorded at each real-time instance. The complete simulation process utilizes the *General

Contact feature to automatically detect all potential contact surfaces. For each identified pair of contact surfaces, a normal hard contact and a tangential frictionless contact are established.

In dynamic explicit finite element analysis, the viscous pressure load $p = C_v \times \rho c_d$ is commonly used as damping to mitigate numerical oscillations, where C_v is the viscous pressure coefficient, ρ and c_d
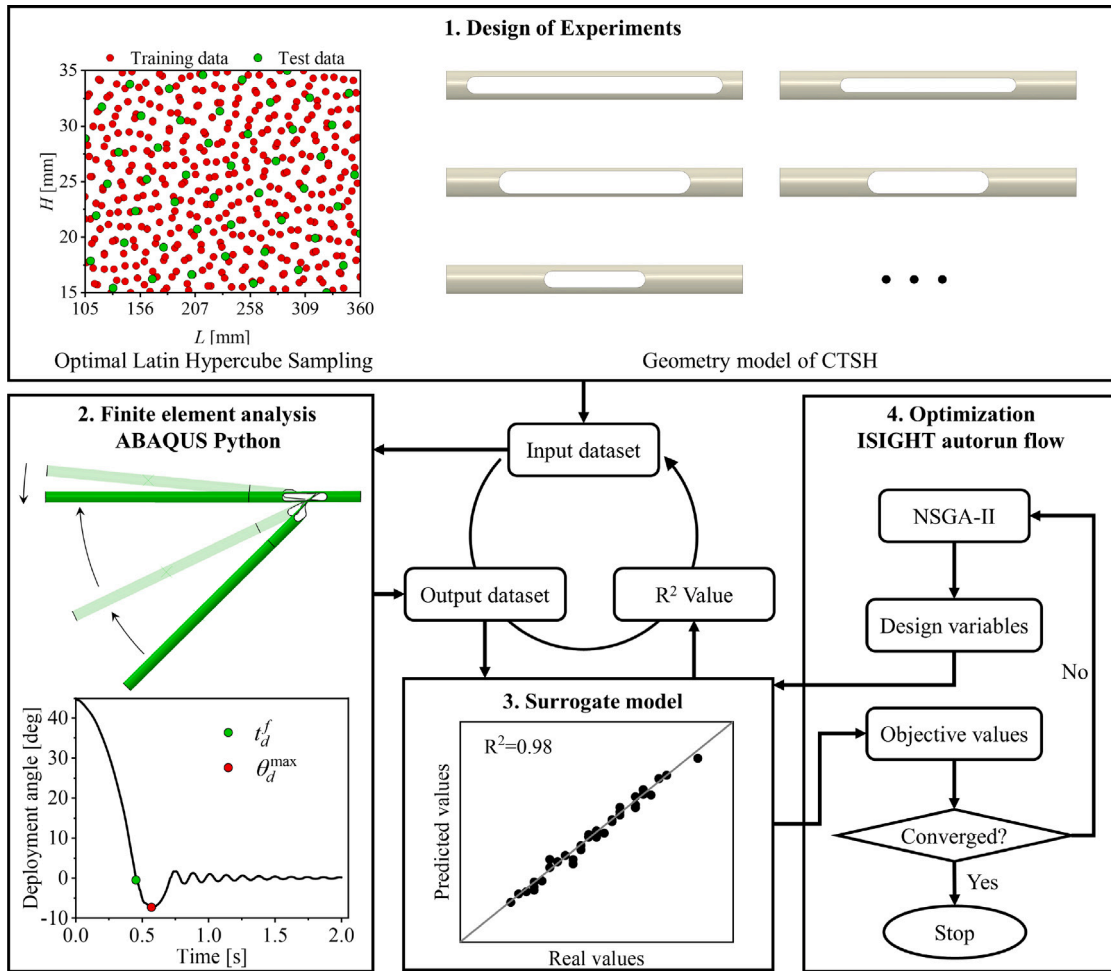
Fig. 8. Flowchart of the surrogate modeling and optimization process. (For interpretation of the references to color in this figure legend, the reader is referred to the web version of this article.)
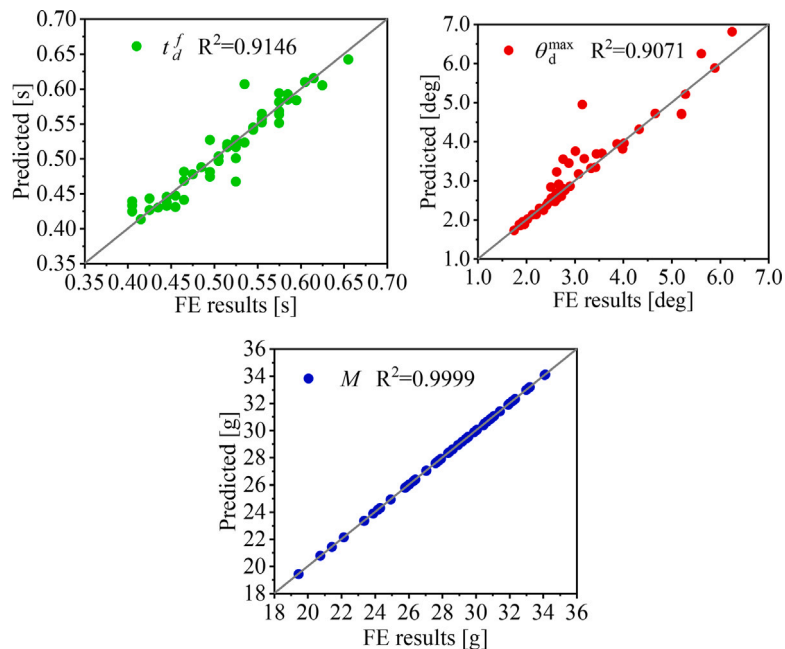

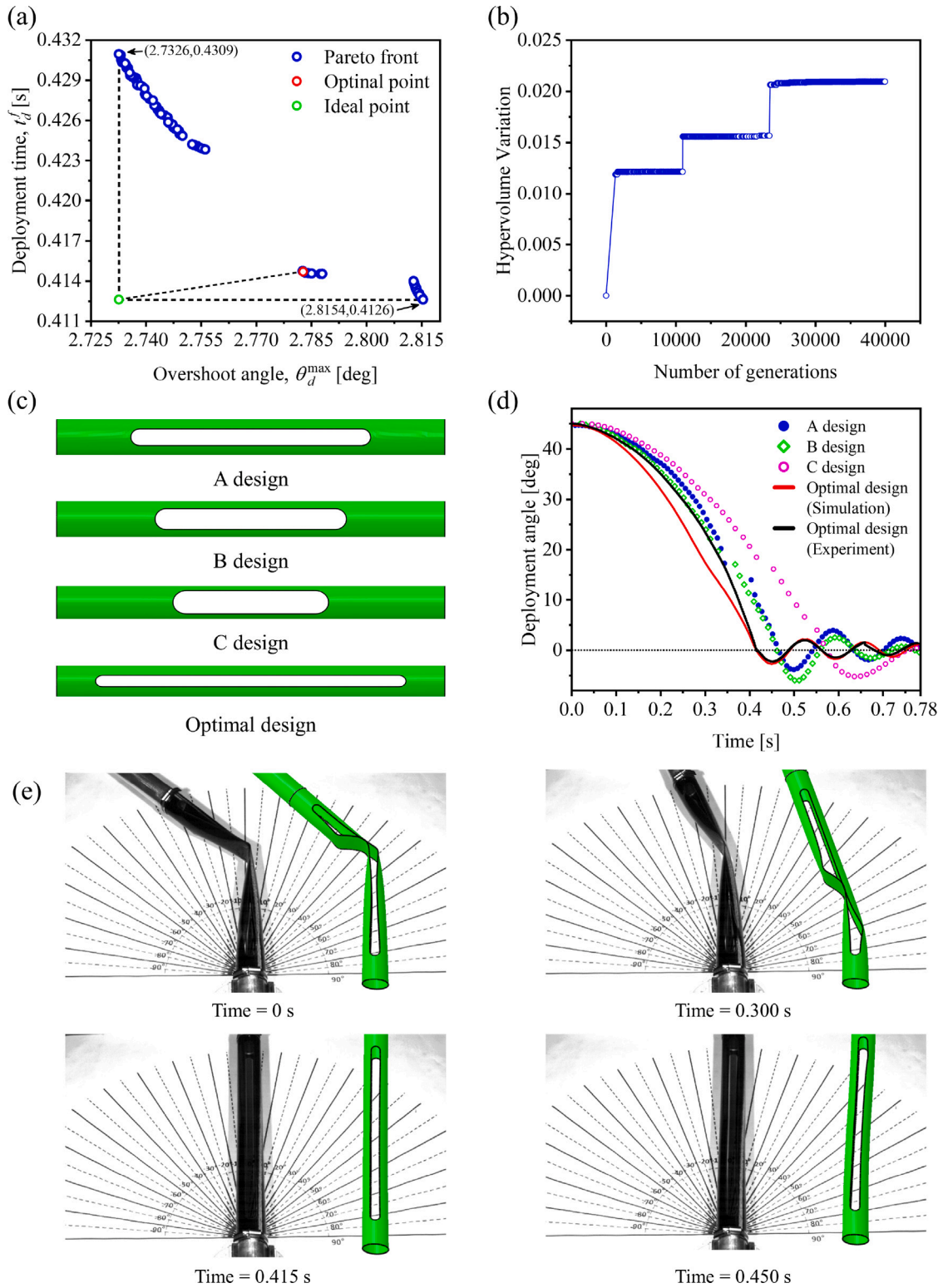**Fig. 9.** Evaluation the accuracy of surrogate model.

Fig. 10. Optimal cutout design obtained through size optimization. (a) Pareto frontier obtained from NGSAII-RBF by minimum the Objectives, t_d^f and θ_d^{max}. (b) Hypervolume variation with an increasing number of generations for evaluating the convergence of the Pareto front. (c) Four configurations: Initial designs (A, B, and C) and the optimized design. (d) Comparison of the time-dynamic unfolding angle curves between initial and optimized designs, where the red curve and black curve represent the simulation and experimental results of the optimized design. (e) Comparison of the optimal CTSH experimental deformation states with the simulation deformation states at different moments of deployment. (For interpretation of the references to color in this figure legend, the reader is referred to the web version of this article.)

denote material properties which are density and wave speed of the material, respectively. Previous research has shown the significant impact of C_v on the quasi-static and dynamic deployment behavior of the CTSH, highlighting the need for careful selection of numerical

values to ensure the accuracy of the simulation model [9,39,40]. The folding process is quasi-static, and the viscous pressure coefficient C_v^f was introduced to damp out the kinetic energy and ensure that the work done by external forces is transformed into the strain energy stored

Table 3
Comparison between experiments and FE solutions for Design C.

	Index	Experiment	FE	Error
Case 1	t_d^f [s]	0.573	0.576	0.52%
	$\theta_d^{\max}$ [deg]	4.987	5.230	4.9%
Case 2	t_d^f [s]	0.480	0.452	5.8%
	$\theta_d^{\max}$ [deg]	6.225	7.298	17.2%

in the deformation. Therefore C_v^f was determined by monitoring the kinetic energy as a small percent of the stored strain energy during the folding process. Through a trial-and-error process, C_v^f was set to 1.4×10^{-7} for *Case 1* and 1.4×10^{-6} for *Case 2* for the designs with two potential folding configurations. Other designs with only unique central folding configurations were assigned $C_v^f = 1.4 \times 10^{-7}$. On the other hand, the deployment process is transient dynamic, for which the viscous damping has a prominent effect on the response of the structure. The viscous pressure coefficient $C_v^d = 5.6 \times 10^{-7}$ was determined through a comparison between simulations and experiments to ensure a good correlation between them in deployment time and overshoot angle.

In Fig. 6, we verified the simulations against experimental data using Design C as an example. Figs. 6(a) and 6(b) depict the energy variations during the quasi-static folding and dynamic deployment processes of the CTSH for the two folding configurations (*Case 1* and *Case 2*). Both cases demonstrate energy conservation during the folding process, where the kinetic energy constitutes less than 5% of the total internal energy, satisfying the criteria for quasi-static conditions. A higher value of C_v^f leads to smoother changes in kinetic energy for *Case 2*. The slight difference in kinetic energy causes the CTSH to adopt different folding configurations after buckling, which is consistent with the findings of Mallikarachchi et al. [9]. It can be seen from Figs. 6(a) and 6(b) that the stored strain energies of *Case1* and *Case2* at the fully folded state are the same. In addition to the fact that in *Case 2* the boom is effectively shorter and hence its moment of momentum after the latching attempt is lower and the moment of inertia about its center of rotation is also lower. Hence, in *Case 2*, the boom will rotate faster and achieve a larger overshoot angle than *Case 1*. A quantitative comparison between the two cases in terms of deployment time and overshoot angle is given in Table 3. Specifically, *Case 2* registers a 19.38% decrease in deployment time t_d^f (0.480 s compared to 0.573 s in *Case 1*) but a 24.82% increase in overshoot angle $\theta_d^{\max}$ (6.225 deg versus 4.987 deg for *Case 1*). Figs. 6(c) and 6(d) provide a comparison between simulation and experimental results for the dynamic deployment of CTSH Design C in both *Case 1* and *Case 2*. The comparison shows excellent agreement. The results for deployment time (t_d^f) and overshoot angle ($\theta_d^{\max}$) are summarized and compared in Table 3. It can be seen that the simulation predicts an accurate deployment time while predicting a slightly larger overshoot angle than the experiment. The discrepancy between experiments and simulations is attributed to the assumption of full constraint of the fixed end in simulations. In the experiments, although the tail of CTSH is fixed with the fixture, it experiences shocks that provide a damping effect, suppressing the overshoot and vibrations to some extent.

Once the general mechanical mechanism of CTSH dynamic deployment was identified, we proceeded to construct a design space to explore the evolution of the deployment time t_d^f and maximum overshoot angle $\theta_d^{\max}$ with respect to the design variables L and H. The diameter of the semi-circles at the ends of the cutouts remains equal to H. Specifically, using the optimal Latin hypercube [41] sampling method, we uniformly sampled 50 sets of cutout design combinations within the intervals of $L \in [105, 360]$ and $H \in [15, 35]$, and calculated the corresponding dynamic responses using the aforementioned high-fidelity finite element model. We would like to note that in all simulations the values of C_v^f and C_v^d are kept constant at 1.4×10^{-7} and 5.6×10^{-7} respectively. Fig. 7(a) illustrates the evolution of t_d^f as a function of L and H. However, the minimum value of t_d^f does not

correspond to the minimum values of L and H. Instead, it occurs in two local minima regions: $L \in [130, 170]$, $H \in [20, 22]$ and $L \in [210, 260]$, $H \in [17, 20]$. Fig. 7(b) presents the evolution of $\theta_d^{\max}$ as a function of L and H. It demonstrates a strong negative correlation between $\theta_d^{\max}$ and both L and H. However, a local minimum value is observed within the region of $L \in [170, 210]$, $H \in [17, 20]$. Fig. 7(c) illustrates the influence of L and H on the mass M of the CTSH, revealing a single negative correlation for each design variable. In conclusion, within the design space mentioned above, a contradiction exists between $\theta_d^{\max}$ and t_d^f, and there is also nonlinearity between the design variables and optimization objectives. Intuitively obtaining the optimal design that minimizes both t_d^f and $\theta_d^{\max}$ simultaneously is not possible. Multi-objective optimization offers a general solution to this problem. It is important to note that in the presence of a design space with multiple local optima (as depicted in Fig. 7(a)), employing global optimization algorithms (e.g., genetic algorithms [42], simulated annealing [43], particle swarm optimization [44]) has become a common approach to avoid being trapped in local regions during the exploration process. Nevertheless, these advanced algorithms require a transient burst of iterations. Modeling the whole quasi-static folding–dynamic unfolding process is time-consuming, and the running typically takes about 1.5 h to complete on a workstation with an Intel (R) Xeon (R) Platinum 8375C 64 - core CPU operating at a frequency of 3.5 GHz. Optimization of this hinge is thus prohibitively computer-intensive, and surrogate modeling is desperately needed.

3. Surrogate modeling and size optimization of CTSH

3.1. Multi-objective optimization problem description

We now describe the multi-objective size optimization problem of the CTSH with a rigorous mathematical formulation, it can be given as:

$$
\begin{cases}
\text{Find}: \ L, H \\
\text{Minimize}: \ t_d^f \\
\text{Minimize}: \ \theta_d^{\max} \\
\text{Subject to}: \ M = 29.94 \pm 0.3 \ [\text{g}]
\end{cases}
\tag{1}
$$

where the L and H are the two design variables, which are, respectively, allowed to vary in the following ranges: $H \in [15, 35]$ and $L \in [105, 360]$, as shown in Fig. 8. t_d^f is the time during the first deployment of CTSH from a 45 degrees folding configuration, and the $\theta_d^{\max}$ is the maximum overshoot angle. These two objective functions are set as the multi-objectives that should be minimized. The mass nearly equaled to 29.94 ± 0.3 g was used as a constraint.

3.2. Surrogate-model-based size optimization framework

The size optimization framework based on surrogate models consists of four steps, as shown in Fig. 8. The first step is the design of experiments (DOE), where the optimal Latin hypercube technique is used to create the design space. The DOE study was independently conducted twice, yielding two datasets: one for training (400 samples represented by red scatter points in the top-left subplot of Fig. 8) and one for testing (50 samples, as described in Section 2.2, depicted by green scatter points). Subsequently, finite element calculations are executed to generate the necessary data for training and testing the surrogate model. Abaqus/Python scripts were developed to automate the simulation runs for each sampling point. These scripts take the two design variables as inputs, perform high-fidelity simulations, and conduct post-processing on specific outputs, such as the M of the CTSH, $\theta_d^{\max}$, and t_d^f. The third step entails developing a surrogate model utilizing the finite element database to rapidly predict the performance of the CTSH. In this case, a Radial Basis Function (RBF) model was employed to construct the surrogate model. The surrogate model was

implemented offline and imported into the software, Isight 2020. In the fourth step within the Isight environment, the NSGA-II multi-objective genetic algorithm is employed to directly invoke the surrogate model for optimization purposes. The process persists until the convergence criteria of the optimization algorithm are achieved, subsequent to which the optimal solution is generated. The established optimization environment has been proven to be efficient and robust for various optimization problems, whether linear or nonlinear. A recent example involves the shape optimization of CTSH quasi-static folding and deployment performance [45], and the data and codes for constructing the surrogate models and optimization framework have been openly shared in the paper. The common adaptability of this optimization strategy is once again emphasized through the work presented in this paper.

3.3. Construction of surrogate model of CTSH

Based on a given set of sample data $\mathbf{x}_1$, $\mathbf{x}_2$, $\cdots$, $\mathbf{x}_n$, and the corresponding observations y_1, y_2, $\cdots$, y_n, RBF is commonly used to construct a function approximation of the following form [46]:

$$y(\mathbf{x}) = \sum_{i=1}^{n} w_i \varphi \left(\left\| \mathbf{x} - \mathbf{c}_i \right\| \right) \tag{2}$$

Where $\mathbf{x}$ represents the prediction point, w_i is the weight coefficient ($\sum_{j=1}^{n} w_i = 0$), and φ denotes the basis function. Available forms of basis functions include linear, cubic, spline, Gaussian, multiquadric, and inverse multiquadric, among others. The notation $\| . \|$ represents the Euclidean distance. The center point $\mathbf{c}_i$ is typically equal to $\mathbf{x}_i$. The computation of $\mathbf{w} = [w_1, w_2, \ldots, w_n]^T$ is performed as follows:

$$\mathbf{w} = \mathbf{H}^{-1} \mathbf{y} \tag{3}$$

The so-called Gram matrix $\mathbf{H}_{i,j} = \varphi \left(\left\| \mathbf{x}^{(i)} - \mathbf{x}^{(j)} \right\| \right), i, j = 1, 2, \ldots, n$ is used to obtained $\mathbf{w}$. By substituting the $\mathbf{w}$ into Eq. (2), the RBF surrogate model is constructed and can predict the response value at any location within the design space. Once the construction of a surrogate model is completed, it is crucial to evaluate the accuracy of the approximation. The R^2 correlation coefficient is used to assess the performance of the surrogate model at m test points. It is calculated using the following equation:

$$R^2 = 1 - \frac{\sum_{i=1}^{m} \left(y_i - \tilde{y}_i \right)^2}{\sum_{i=1}^{m} \left(y_i - \bar{y} \right)^2} \tag{4}$$

Where y_i represents the test data of the i th sample point, $\tilde{y}_i$ is the prediction made by the surrogate model at the corresponding locations of the test data, and $\bar{y}$ is the mean value of y_i for $i = 1, 2, \ldots, m$.

3.4. Fitting accuracy of surrogate model

Fig. 9 depicts the predictions of the surrogate model and the corresponding actual finite element results. The straight line represents a perfect prediction with zero error, while the degree of dispersion and deviation from this line is quantitatively characterized by the R^2 measure included in each graph. Generally, as R^2 approaches 1, the accuracy of the surrogate values improves. The surrogate model performs exceptionally well in terms of accuracy, with R^2 measurements approaching 100% for the mass. There is slightly larger variation between the predicted and test data for $\theta_d^{\max}$ and t_d^f, but still at least 90% R^2 measures. It is important to note that surrogate model-assisted optimization always aims for the highest possible fitting accuracy. However, achieving even minor improvements in fitting accuracy may necessitate a significant increase in the amount of training data for the model [47], leading to excessive computational costs. Finding a balance between computational costs and fitting accuracy is a reasonable and more feasible approach.

4. Results

An analysis of Fig. 7 revealed a fundamental conflict between Objectives, as laid out in Eq. (1). This conflict makes it challenging to find a unique optimal solution for the problem. To address this issue, we employed the NSGA-II algorithm, augmented with an RBF surrogate model. The algorithm in Isight was configured with 40,000 iterations and a population size of 20, conducting 2000 generations per population (for additional settings about optimization algorithm, refer to the supplementary link). The resulting Pareto front is illustrated in Fig. 10(a). To evaluate the convergence of the Pareto solution set, we utilized Hypervolume as a metric [48]. The Hypervolume is computed as the union of the hypercuboids formed by each Pareto solution and a pre-defined reference point, usually chosen to be inferior to all solutions in the Pareto front, and in this study, it is set at (2.9154, 0.5310). As the iterations progress, an increasing number of solutions populate the Pareto front, thereby increasing the Hypervolume. Fig. 10(b) shows that the Hypervolume has stabilized after 40,000 iterations, equivalent to 40,000 function evaluations. This finding underscores the necessity of employing a surrogate model, given the high computational cost of the simulations. Furthermore, our Pareto front, as depicted in Fig. 10(a), exhibits gaps. This phenomenon is attributed to the presence of multiple local optima in the design space for both t_d^f and θ_d^{max} [49]. This underscores that gradient-based optimization techniques are ill-suited for this problem. Finally, we applied the Ideal Point method to identify the most optimal solution within the Pareto front [50]. The ideal point, marked in green in Fig. 10(a), was located at coordinates (2.7326, 0.4126). The optimal solution, denoted by a red point in the same figure, was determined based on its proximity to the ideal point. The dimension parameters for this optimal solution are labeled as $L = 336.31$ mm, $H = 15.75$ mm. Fig. 10(c) displays the optimal cutout design for CTSH. Table 4 compares the predicted outcomes of the optimization objectives with the FEA results and experimental data. The table illustrates that the error between the RBF predictions and FEA results is a mere 0.678%, underscoring the high accuracy of the surrogate model. Both the FEA and RBF results maintain a maximum relative error of less than 5% compared to the experimental results, confirming the correctness of the optimization outcomes and the reliability of the optimization strategy presented in this paper.

Fig. 10(d) compares the dynamic deployment performance of the initial designs (referred to as Designs A, B, and C as mentioned earlier) with the optimized design. From Fig. 10(d), it is evident that the optimized design yields significant improvements in both optimization objectives, $\theta_d^{\max}$ and t_d^f, compared to the three initial designs. Table 5 presents a quantitative comparison of the specific values for the three initial designs and the optimized design. Among the three designs (A, B, and C), Design A demonstrates the fastest deployment time ($\theta_d^{\max}$) and the smallest overshoot angle (t_d^f). The optimal design enhances these two metrics by 26.3% and 12.6%, respectively. A longer and narrower slot results in tape springs with a larger cross-sectional extending angle, allowing them to store more strain energy when folded and provide greater stiffness during deployment. Consequently, the optimal design achieves a concurrent reduction in deployment time and overshoot angle. Additionally, as shown in Figs. 10(d) and 10(e), the experimental and simulation results for the optimal design are in a good agreement in terms of the two objectives, i.e., the deployment time and overshoot angle, although a small discrepancy exists between them.

It is important to highlight that the entire size optimization process can be accomplished using only 450 high-fidelity FEA simulations to generate sample data for training and validating the surrogate model. Given that the time required for training and utilizing the surrogate model (which predicts CTSH performance in less than 1 s) is negligible compared to the time consumed by high-fidelity FEA computations.

Therefore, we emphasize the substantial computational time savings achievable in this CTSH size optimization. Conducting a single high-fidelity FEA simulation takes 1.5 h, and performing 32,000 direct

Table 4
Optimization design validation through predictive, FEA, and experimental results.

	L [mm]	H [mm]	$\theta_d^{\max}$ [deg]	t_d^f [s]	M [g]
RBF	336.31	15.75	2.783	0.415	29.94
FEA	336.31	15.75	2.802	0.415	29.945
Exp.	336.31	15.75	2.672	0.416	30.180

Table 5
Comparison of performance between optimal design and initial designs.

	L [mm]	H [mm]	$\theta_d^{\max}$ [deg]	t_d^f [s]	M [g]
Optimal Design	336.31	15.75	2.802	0.415	29.94
Initial Design A	252	20	3.80	0.475	29.94
Initial Design B	192	25	6.25	0.475	29.71
Initial Design C	146	30	5.05	0.58	29.83

iterations would take 2000 days. However, by running 450 FEA simulations to construct the surrogate model and subsequently conducting 32,000 iterations, the process can be completed in 28 days, leading to a computational cost reduction of over 97%.

5. Conclusions

By incorporating cutouts in resin-based carbon fiber-reinforced composite tubes, they can be ingeniously converted into a straightforward and practical deployable structure called the CTSH. The cutouts take advantage of the flexible characteristics of the composite material, enabling the CTSH to be compressed, folded, and stored for extended durations, and subsequently deployed as required. This concept has contributed to the advancement of diverse deployable structures that rely on the CTSH as a fundamental element. The dynamic deployment of the CTSH is a crucial maneuver during its in-orbit operation, posing challenges attributed to the complex nonlinear behavior of the structure. Despite extensive research on CTSH deployment encompassing design, analysis, and experimental investigations, the exploration of enhancing the dynamic deployment performance of CTSH through cutout design remains unexplored.

To elucidate the efficacy of cutout design in enhancing CTSH deployment dynamics, dynamic deployment tests were performed on booms with CTSH at the root. Subsequently, high-fidelity simulation models were established using Abaqus/Explicit finite element software, considering the obtained test results. Conclusions were drawn based on the experimental data and parametric simulation analysis: (1) CTSH with identical mass and capsule-shaped cutouts exhibits a notable nonlinear correlation between the longitudinal or transverse cutout dimensions and both the deployment time and maximum overshoot angle. (2) Deployment time and maximum overshoot angle demonstrate contradictory behaviors. This observation underscores the need for multi-objective cutout size optimization in CTSH.

In structural optimization problems, hundreds or thousands of iterations are necessary. However, performing high-fidelity finite element analyses for each structural response or objective function evaluation would be highly time-consuming and computationally intensive.

In this study, an integrated approach combining data-driven surrogate modeling and size optimization was employed to address the aforementioned problem. The framework consists of seamlessly integrating an offline data-driven surrogate modeling process and an online optimization process. A limited number of data points for design variables were sampled using Latin hypercube sampling, and the RBF surrogate model was constructed by evaluating the structural response with finite element analyses. The surrogate model was utilized as a substitute for the genetic algorithm-based optimizer, eliminating the requirement for high-fidelity finite element analyses to evaluate all objective functions during the optimization process. For the CTSH size optimization problem investigated in this study, this method resulted in computational time savings of over 97% and conservative reductions of

26.3% and 12.6% in maximum overshoot angle and deployment time, respectively.

In summary, this work provides an accelerated optimization framework based on surrogate modeling. This framework is designed to enhance the deployment dynamic performance of deployable composite structures by optimizing the cut-out size. It is important to note that the framework proposed here is readily extendable to address various other optimization problems related to deployable composite structures. Specifically, the framework can be extended to include optimization of composite fiber orientation and layup configuration as design variables. The optimization objectives can be broadened to enhance multiple aspects of the performance of deployable composite structures, such as structural integrity, stiffness, strength, stability, shock from deploying CTSH on the satellite, and other factors relevant to the specific mission requirements. To ensure the safety and reliability of the deployable composite structures, the framework may take into account failure mechanisms for composites as constraints in the optimization problem. In addition, it has been demonstrated that the viscoelastic–plastic behavior of composite materials can significantly impact the performance of space deployable structures [10,34,51]. This is particularly relevant for structures that demand high surface accuracy, such as space deployable antennas and telescopes. Therefore, future work should take into account the viscoelastic–plastic behavior of high-strain composite deployable structures to ensure the precise recovery of space mechanisms.

CRediT authorship contribution statement

Hao Jin: Writing – original draft, Validation, Software, Methodology, Investigation, Formal analysis, Data curation. **Ning An:** Writing – review & editing, Writing – original draft, Resources. **Qilong Jia:** Writing – review & editing, Supervision. **Ruiwen Guo:** Validation, Investigation, Data curation. **Xiaofei Ma:** Writing – review & editing, Supervision. **Jinxiong Zhou:** Writing – review & editing, Supervision, Resources.

Declaration of competing interest

The authors declare that they have no known competing financial interests or personal relationshipsthat could have appeared to influence the work reported in this paper.

Data availability

The source codes for dynamic deployment finite element models of CTSH, as well as the construction of surrogate and optimization platforms, are openly available. They can be accessed and downloaded from https://github.com/XJTU-Zhou-group/Size-Optimization-of-CTSH.

Acknowledgments

References

[1] M. Silver, J. Hinkle, L. Peterson, Modeling of snap-back bending response of doubly slit cylindrical shells, in: 45th AIAA/ASME/ASCE/AHS/ASC Structures, Structural Dynamics & Materials Conference, 2004, p. 1820.
[2] M. Silver, J. Hinkle, L. Peterson, Controlled displacement snap-through of tape springs: modeling and experiment, in: 46th AIAA/ASME/ASCE/AHS/ASC Structures, Structural Dynamics and Materials Conference, 2005, p. 2314.

[3] J. Footdale, J. Banik, T. Murphey, Design developments of a non-planar deployable structure, in: 51st AIAA/ASME/ASCE/AHS/ASC Structures, Structural Dynamics, and Materials Conference 18th AIAA/ASME/AHS Adaptive Structures Conference 12th, 2010, p. 2608.

[4] S. Ferraro, S. Pellegrino, Topology and shape optimization of ultrathin composite self-deployable shell structures with cutouts, AIAA J. 59 (9) (2021) 3696–3709.

[5] A. Lopatin, E. Morozov, Z. Kazantsev, N. Berdnikova, Deployment analysis of a composite thin-walled toroidal rim with elastic hinges: Application to an umbrella-type reflector of spacecraft antenna, Compos. Struct. 306 (2023) 116566.

[6] M. Mobrem, D.S. Adams, Deployment analysis of the lenticular jointed antennas onboard the mars express spacecraft, J. Spacecr. Rockets 46 (2) (2009) 394–402.

[7] D.S. Adams, M. Mobrem, Lenticular jointed antenna deployment anomaly and resolution onboard the mars express spacecraft, J. Spacecr. Rockets 46 (2) (2009) 403–410.

[8] European Space Agency, Jupiter Icy Moons Explorer, 2023, https://www.esa.int/Science_Exploration/Space_Science/Juice.

[9] H. Mallikarachchi, S. Pellegrino, Deployment dynamics of ultrathin composite booms with tape-spring hinges, J. Spacecr. Rockets 51 (2) (2014) 604–613.

[10] K. Kwok, S. Pellegrino, Folding, stowage, and deployment of viscoelastic tape springs, AIAA J. 51 (8) (2013) 1908–1918.

[11] M. Mobrem, D.S. Adams, Deployment analysis of the lenticular jointed antennas onboard the mars express spacecraft, J. Spacecr. Rockets 46 (2) (2009) 394–402.

[12] D.S. Adams, M. Mobrem, Lenticular jointed antenna deployment anomaly and resolution onboard the mars express spacecraft, J. Spacecr. Rockets 46 (2) (2009) 403–410.

[13] J. Block, M. Straubel, M. Wiedemann, Ultralight deployable booms for solar sails and other large gossamer structures in space, Acta Astronaut. 68 (7–8) (2011) 984–992.

[14] D. Jinfeng, A. Ning, J. Qilong, M. Xiaofei, Deployment analysis of composite thin-walled lenticular tubes with effect of storage time and temperature, Chin. J. Aeronaut. (2023).

[15] H. Mallikarachchi, S. Pellegrino, Design of ultrathin composite self-deployable booms, J. Spacecr. Rockets 51 (6) (2014) 1811–1821.

[16] H. Ye, Y. Zhang, Q. Yang, Y. Xiao, R.V. Grandhi, C.C. Fischer, Optimal design of a three tape-spring hinge deployable space structure using an experimentally validated physics-based model, Struct. Multidiscip. Optim. 56 (2017) 973–989.

[17] H. Yang, R. Liu, Y. Wang, Z. Deng, H. Guo, Experiment and multiobjective optimization design of tape-spring hinges, Struct. Multidiscip. Optim. 51 (2015) 1373–1384.

[18] T.-W. Liu, J.-B. Bai, N. Fantuzzi, G.-Y. Bu, D. Li, Multi-objective optimisation designs for thin-walled deployable composite hinges using surrogate models and Genetic Algorithms, Compos. Struct. 280 (2022) 114757.

[19] S. Ferraro, S. Pellegrino, Topology and shape optimization of ultrathin composite self-deployable shell structures with cutouts, AIAA J. 59 (9) (2021) 3696–3709.

[20] H. Jin, Q. Jia, N. An, G. Zhao, X. Ma, J. Zhou, Surrogate modeling accelerated shape optimization of deployable composite tape-spring hinges, AIAA J. 60 (10) (2022) 5942–5953.

[21] P. Fernandes, R. Pinto, A. Ferrer, N. Correia, Performance analysis of a damage tolerant composite self-deployable elastic-hinge, Compos. Struct. 288 (2022) 115407.

[22] M. Mobrem, D.S. Adams, Deployment analysis of the lenticular jointed antennas onboard the mars express spacecraft, J. Spacecr. Rockets 46 (2) (2009) 394–402.

[23] D.S. Adams, M. Mobrem, Lenticular jointed antenna deployment anomaly and resolution onboard the mars express spacecraft, J. Spacecr. Rockets 46 (2) (2009) 403–410.

[24] F. Li, L. Liu, L. Du, Y. Liu, J. Leng, Mechanical analysis of a tip-loaded deployable truss based on shape memory polymer composite, Compos. Struct. 242 (2020) 112196.

[25] S.S. Lakshmi, M. Varsha, G.S. Krishnaa, V.M. Kuriakose, S.M. Subhani, H.S. Subramanian, V. Sreehari, Thermo-structural analysis of deployable composite booms with slotted hinges for space applications, Mater. Today Proc. 56 (2022) 3564–3570.

[26] H. Mallikarachchi, S. Pellegrino, Quasi-static folding and deployment of ultrathin composite tape-spring hinges, J. Spacecr. Rockets 48 (1) (2011) 187–198.

[27] H. Mallikarachchi, S. Pellegrino, Deployment dynamics of ultrathin composite booms with tape-spring hinges, J. Spacecr. Rockets 51 (2) (2014) 604–613.

[28] A. Sobester, A. Forrester, A. Keane, Engineering Design Via Surrogate Modelling: A Practical Guide, John Wiley & Sons, 2008.

[29] T.W. Simpson, T.M. Mauery, J.J. Korte, F. Mistree, Kriging models for global approximation in simulation-based multidisciplinary design optimization, AIAA J. 39 (12) (2001) 2233–2241.

[30] S. Jeong, M. Murayama, K. Yamamoto, Efficient optimization design method using kriging model, J. Aircraft 42 (2) (2005) 413–420.

[31] N.V. Queipo, R.T. Haftka, W. Shyy, T. Goel, R. Vaidyanathan, P.K. Tucker, Surrogate-based analysis and optimization, Prog. Aerosp. Sci. 41 (1) (2005) 1–28.

[32] F.A. Viana, T.W. Simpson, V. Balabanov, V. Toropov, Special section on multidisciplinary design optimization: metamodeling in multidisciplinary design optimization: how far have we really come? AIAA J. 52 (4) (2014) 670–690.

[33] J.R. Davis, et al., ASM Specialty Handbook: Tool Materials, ASM international, 1995.

[34] N. An, Q. Jia, H. Jin, X. Ma, J. Zhou, Multiscale modeling of viscoelastic behavior of unidirectional composite laminates and deployable structures, Mater. Des. 219 (2022) 110754.

[35] The MathWorks Inc., Image processing toolbox, 2022, URL https://ww2.mathworks.cn/help/images/ref/hough.html.

[36] R.O. Duda, P.E. Hart, Use of the hough transformation to detect lines and curves in pictures, Commun. ACM 15 (1) (1972) 11–15.

[37] SKYFLEX, Materials selection guide, 2014, Document No. SKPP-MSG, Version 2.0.

[38] Abaqus, Inc, ABAQUS/Explicit User's Manual, Dassault Systèmes Simulia Corp., Providence, RI, USA, 2020.

[39] H. Mallikarachchi, S. Pellegrino, Quasi-static folding and deployment of ultrathin composite tape-spring hinges, J. Spacecr. Rockets 48 (1) (2011) 187–198.

[40] Q. Jia, N. An, X. Ma, J. Zhou, A dynamic finite element procedure for bending collapse of composite thin-walled lenticular tubes, Compos. Struct. 287 (2022) 115364.

[41] J.-S. Park, Optimal Latin-hypercube designs for computer experiments, J. Statist. Plann. Inference 39 (1) (1994) 95–111.

[42] S. Mirjalili, S. Mirjalili, Genetic algorithm, Evol. Algorithms Neural Netw.: Theory Appl. (2019) 43–55.

[43] A. Suppapitnarm, K.A. Seffen, G.T. Parks, P. Clarkson, A simulated annealing algorithm for multiobjective optimization, Eng. Optim. 33 (1) (2000) 59–85.

[44] F. Marini, B. Walczak, Particle swarm optimization (PSO). A tutorial, Chemometr. Intell. Lab. Syst. 149 (2015) 153–165.

[45] H. Jin, Q. Jia, N. An, G. Zhao, X. Ma, J. Zhou, Surrogate modeling accelerated shape optimization of deployable composite tape-spring hinges, AIAA J. 60 (10) (2022) 5942–5953.

[46] M.D. Buhmann, Radial basis functions, Acta Numer. 9 (2000) 1–38.

[47] A.J. Keane, I.I. Voutchkov, Surrogate approaches for aerodynamic section performance modeling, AIAA J. 58 (1) (2020) 16–24.

[48] N. Beume, C.M. Fonseca, M. Lopez-Ibanez, L. Paquete, J. Vahrenhold, On the complexity of computing the hypervolume indicator, IEEE Trans. Evol. Comput. 13 (5) (2009) 1075–1082.

[49] M. Bessa, S. Pellegrino, Design of ultra-thin shell structures in the stochastic post-buckling range using Bayesian machine learning and optimization, Int. J. Solids Struct. 139 (2018) 174–188.

[50] F. Bre, V.D. Fachinotti, A computational multi-objective optimization method to improve energy efficiency and thermal comfort in dwellings, Energy Build. 154 (2017) 283–294.

[51] P. Fernandes, B. Sousa, R. Marques, J.M.R. Tavares, A. Marques, R.N. Jorge, R. Pinto, N. Correia, Influence of relaxation on the deployment behaviour of a cfrp composite elastic–hinge, Compos. Struct. 259 (2021) 113217.